# Partial Fourier techniques in single-shot cross-term spatiotemporal encoded MRI

# Magnetic Resonance in Medicine

Copy of e-mail Notification



Dear Author,

Your article page proofs for Magnetic Resonance in Medicine are ready for review. John Wiley & Sons has made this article available to you online for faster, more efficient editing. Please follow the instructions below and you will be able to access a PDF version of your article as well as relevant accompanying paperwork.

First, make sure you have a copy of Adobe Acrobat Reader software to read these files. This is free software and is available for user downloading at http://www.adobe.com/products/acrobat/readstep.html.

Open your web browser, and enter the following web address:
http://cps.kwglobal.com/jw/retrieval.aspx?pwd=fe5a401b1743

You will be prompted to log in, and asked for a password. Your login name will be your email address, and your password will be fe5a401b1743

Example:

Login: your e-mail address
Password: fe5a401b1743

The site contains two files, containing:

- Author Instructions Checklist
- Adobe Acrobat Users - NOTES tool sheet
- Reprint Order Information
- A copy of your page proofs for your article

You will also find a PDF showing a redlined version of your manuscript, which shows the changes introduced in copyediting. This has been included for your reference, but you do not need to edit or return the redlined manuscript.

Please complete these forms electronically. (If you do not wish to order reprints, please mark a "0" on the reprint order form.) Read your page proofs carefully and:

- make any necessary changes or corrections
- answer all queries (footnotes A,B,C, etc.) on the last page of the PDF proof
- proofread any tables and equations carefully

- check your figure legends for accuracy

Within 48 hours, please return all materials via e-mail to MRM@wiley.com. This will include:

1) Page proofs with corrections

Return to:
MRM Production Team
E-mail: MRM@wiley.com

Technical problems? If you experience technical problems downloading your file or any other problem with the website listed above, please contact Balaji (e-mail: Wiley.CS@cenveo.com, phone: +91 (44) 4205-8810 (ext.308)). Be sure to include your article number.

Questions regarding your article? Please don't hesitate to contact the MRM Production Team at mrm@wiley.com with any questions about the article itself, or if you have trouble interpreting any of the questions listed at the end of your file. REMEMBER TO INCLUDE YOUR ARTICLE NO. ( 26824 ) WITH ALL CORRESPONDENCE. This will help both of us address your query most efficiently.

As this e-proofing system was designed to make the publishing process easier for everyone, we welcome any and all feedback. Thanks for participating in our e-proofing system!

This e-proof is to be used only for the purpose of returning corrections to the publisher.

Your article cannot be published until we have received your completed license agreement. If you have not already done so, please log in into Author Services (https://authorservices.wiley.com) and click on "My Dashboard." When you locate your article on the Dashboard, please click the button that says "Sign License" to use the Wiley Author Licensing Service (WALS) to complete your license agreement.

Sincerely,

MRM Production Team
E-mail: MRM@wiley.com

Magnetic Resonance in Medicine

Copy of e-mail Notification


111 River Street, Hoboken, NJ 07030

*****IMMEDIATE RESPONSE REQUIRED*****

Your article will be published online via Wiley's EarlyView® service (www.interscience.wiley.com) shortly after receipt of corrections. EarlyView®is Wiley's online publication of individual articles in full text HTML and/or pdf format before release of the compiled print issue of the journal. Articles posted online in EarlyView® are peer-reviewed, copyedited, author corrected, and fully citable via the article DOI (for further information, visit www.doi.org). EarlyView® means you benefit from the best of two worlds—fast online availability as well as traditional, issue based archiving.

Please follow these instructions to avoid delay of publication.

**READ PROOFS CAREFULLY**

- This will be your only chance to review these proofs. **Please note that once your corrected article is posted online, it is considered legally published, and cannot be removed from the Web site for further corrections.**
- Please note that the volume and page numbers shown on the proofs are for position only.

**ANSWER ALL QUERIES ON PROOFS** (Queries for you to answer are attached as the last page of your proof.)

- Mark all corrections directly on the proofs. Note that excessive alterations may ultimately result in delay of publication and extra costs may be charged to you.

**CHECK FIGURES AND TABLES CAREFULLY**

- Check size, numbering, and orientation of figures.
- All images in the PDF are downsampled (reduced to lower resolution and file size) to facilitate Internet delivery. These images will appear at a higher resolution and sharpness in the printed article.
- Review figure legends to ensure that they are complete.
- Check all tables. Review layout, title, and footnotes.

**RETURN PROOFS**
**CTA (If you have not already signed one)**

**RETURN IMMEDIATELY AS YOUR ARTICLE WILL BE POSTED ONLINE SHORTLY AFTER RECEIPT.**
**E-MAIL TO: MRM@wiley.com**

**QUESTIONS?**

**MRM Production Team**
E-mail: MRM@wiley.com

---

Refer to journal acronym and article production number
(i.e., MRM 00-00000).

WILEY

# USING e-ANNOTATION TOOLS FOR ELECTRONIC PROOF CORRECTION

**Required software to e-Annotate PDFs: Adobe Acrobat Professional or Adobe Reader (version 8.0 or above). (Note that this document uses screenshots from Adobe Reader DC.)**
**The latest version of Acrobat Reader can be downloaded for free at: http://get.adobe.com/reader/**

Once you have Acrobat Reader open on your computer, click on the Comment tab (right-hand panel or under the Tools menu).

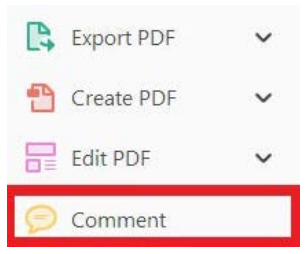


This will open up a ribbon panel at the top of the document. Using a tool will place a comment in the right-hand panel. The tools you will use for annotating your proof are shown below:

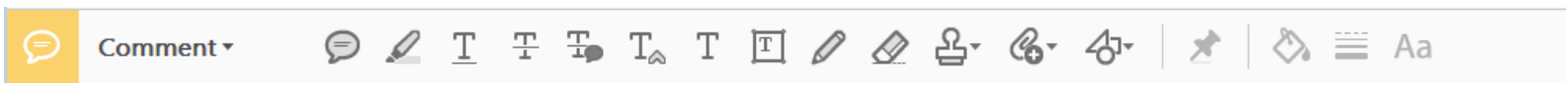


## 1. Replace (Ins) Tool – for replacing text.

Strikes a line through text and opens up a text box where replacement text can be entered.

**How to use it:**

- Highlight a word or sentence.
- Click on .
- Type the replacement text into the blue box that appears.

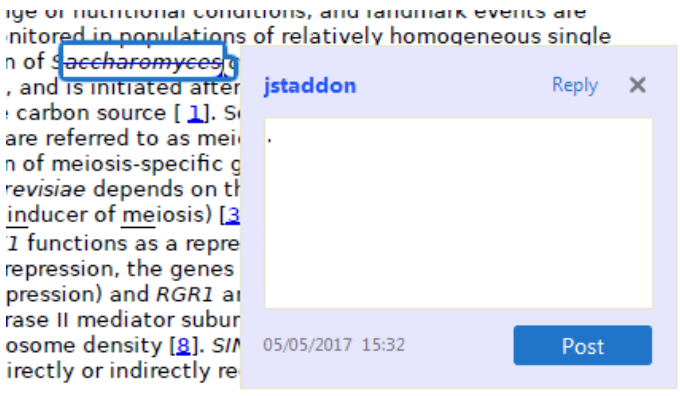


## 2. Strikethrough (Del) Tool – for deleting text.

Strikes a red line through text that is to be deleted.

**How to use it:**

- Highlight a word or sentence.
- Click on .
- The text will be struck out in red.

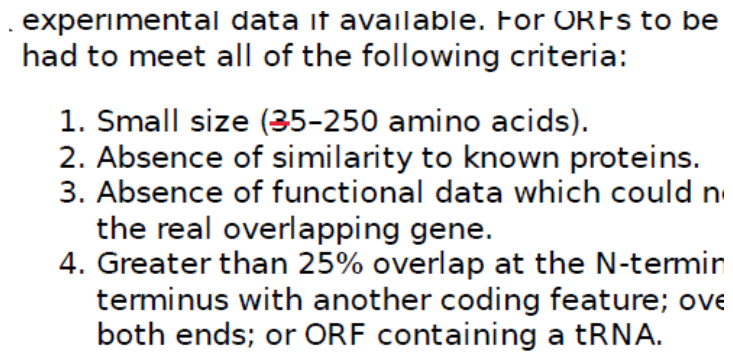
experimental data if available. For ORFs to be had to meet all of the following criteria:

1. Small size (~~3~~5–250 amino acids).
2. Absence of similarity to known proteins.
3. Absence of functional data which could n the real overlapping gene.
4. Greater than 25% overlap at the N-termir terminus with another coding feature; ove both ends; or ORF containing a tRNA.

## 3. Commenting Tool – for highlighting a section to be changed to bold or italic or for general comments.

Use these 2 tools to highlight the text where a comment is then made.

**How to use it:**

- Click on .
- Click and drag over the text you need to highlight for the comment you will add.
- Click on .
- Click close to the text you just highlighted.
- Type any instructions regarding the text to be altered into the box that appears.

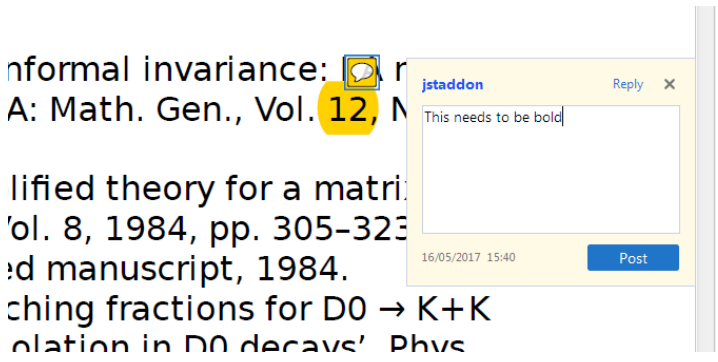


## 4. Insert Tool – for inserting missing text at specific points in the text.

Marks an insertion point in the text and opens up a text box where comments can be entered.

**How to use it:**

- Click on .
- Click at the point in the proof where the comment should be inserted.
- Type the comment into the box that appears.

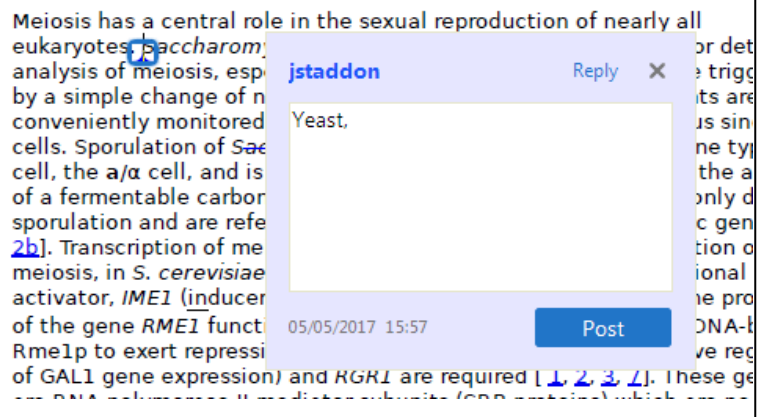

WILEY

# USING e-ANNOTATION TOOLS FOR ELECTRONIC PROOF CORRECTION

## 5. Attach File Tool – for inserting large amounts of text or replacement figures.

Inserts an icon linking to the attached file in the appropriate place in the text.

**How to use it:**

- Click on  .
- Click on the proof to where you'd like the attached file to be linked.
- Select the file to be attached from your computer or network.
- Select the colour and type of icon that will appear in the proof. Click OK.

  The attachment appears in the right-hand panel.

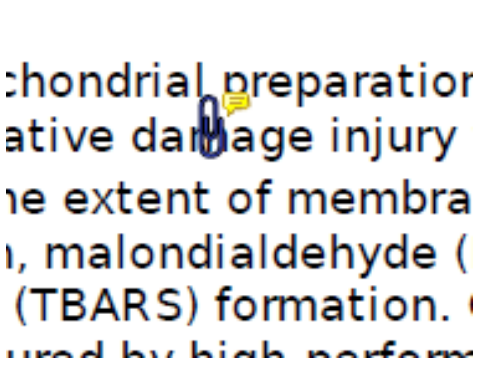


## 6. Add stamp Tool – for approving a proof if no corrections are required.

Inserts a selected stamp onto an appropriate place in the proof.

**How to use it:**

- Click on  .
- Select the stamp you want to use. (The Approved stamp is usually available directly in the menu that appears. Others are shown under *Dynamic*, *Sign Here*, *Standard Business*).
- Fill in any details and then click on the proof where you'd like the stamp to appear. (Where a proof is to be approved as it is, this would normally be on the first page).

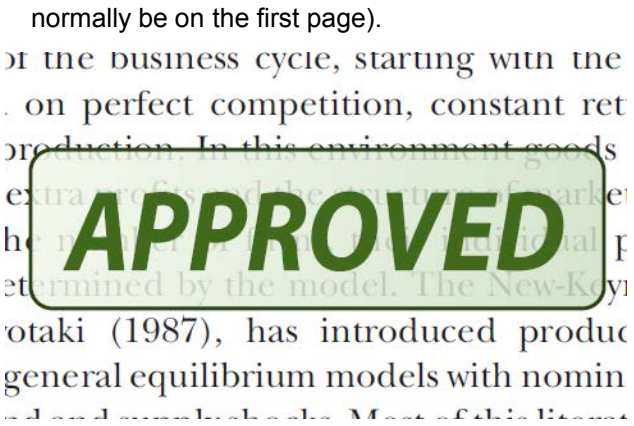


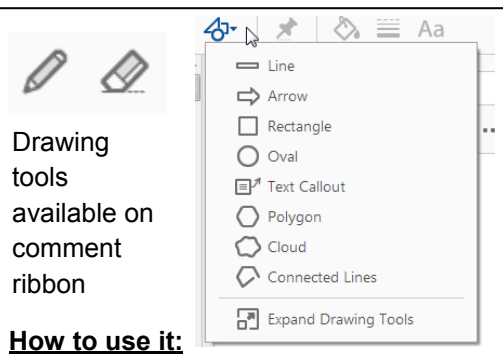

Drawing tools available on comment ribbon




## 7. Drawing Markups Tools – for drawing shapes, lines, and freeform annotations on proofs and commenting on these marks.

Allows shapes, lines, and freeform annotations to be drawn on proofs and for comments to be made on these marks.

**How to use it:**

- Click on one of the shapes in the Drawing Markups section.
- Click on the proof at the relevant point and draw the selected shape with the cursor.
- To add a comment to the drawn shape, right-click on shape and select *Open Pop-up Note.*
- Type any text in the red box that appears.

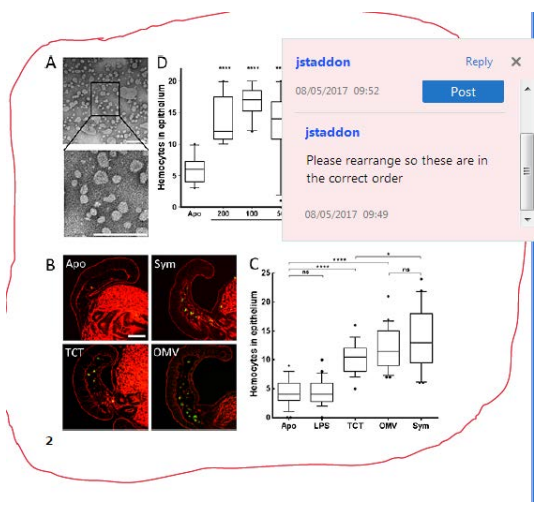


**For further information on how to annotate proofs, click on the Help menu to reveal a list of further options:**

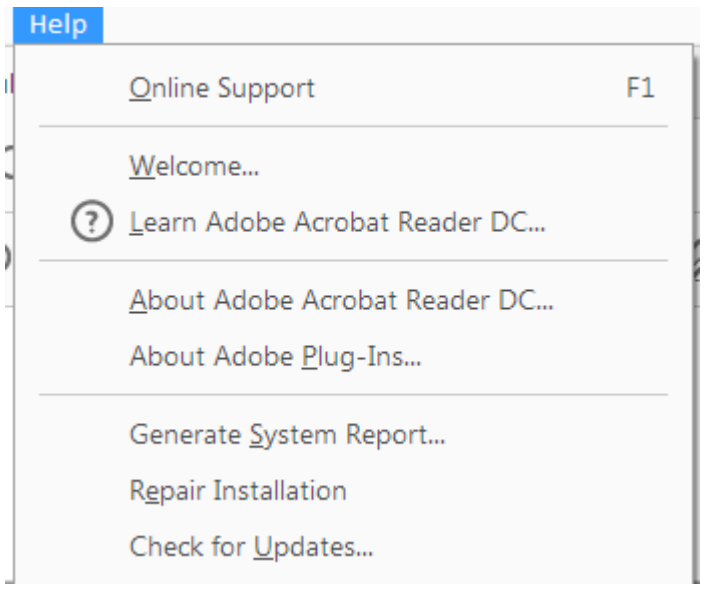

26824 Cadmus Art: MRM26824 Ed. Ref. No.: 17-17848.R2 Date: 30-June-17 Stage: Page: 1

FULL PAPER

Magnetic Resonance in Medicine 00:00–00 (2017)

# Partial Fourier Techniques in Single-Shot Cross-Term Spatiotemporal Encoded MRI

AQ46 Zhiyong Zhang and Lucio Frydman*

**Purpose:** Cross-term spatiotemporal encoding (xSPEN) is a single-shot approach with exceptional immunity to field heterogeneities, the images of which faithfully deliver 2D spatial distributions without requiring a priori information or using postacquisition corrections. xSPEN, however, suffers from AQ7 signal-to-noise ratio penalties due to its non-Fourier nature and due to diffusion losses—especially when seeking high resolution. This study explores partial Fourier transform approaches that, acting along either the readout or the spatiotemporally encoded dimensions, reduce these penalties.

**Methods:** xSPEN uses an orthogonal (e.g., *z*) gradient to read, in direct space, the low-bandwidth (e.g., *y*) dimension. This substantially changes the nature of partial Fourier acquisitions vis-à-vis conventional imaging counterparts. A suitable theoretical analysis is derived to implement these procedures, along either the spatiotemporally or readout axes.

**Results:** Partial Fourier single-shot xSPEN images were recorded on preclinical and human scanners. Owing to their reduction in the experiments' acquisition times, this approach provided substantial sensitivity gains vis-à-vis previous implementations for a given targeted in-plane resolution. The physical origins of these gains are explained.

**Conclusion:** Partial Fourier approaches, particularly when implemented along the low-bandwidth spatiotemporal dimension, provide several-fold sensitivity advantages at minimal costs to the execution and processing of the single-shot experiments. **Magn Reson Med 000:000–000, 2017. © 2017 International Society for Magnetic Resonance in Medicine.**

**Key words:** single-shot MRI; spatiotemporal encoding; xSPEN; resolution enhancement; sensitivity enhancement; AQ8 partial Fourier transform

## INTRODUCTION

Cross-term spatiotemporal encoding (xSPEN) is a novel approach delivering single-scan NMR images with unprecedented resilience to field inhomogeneities (1). Like its spatiotemporally encoded (SPEN) predecessors (2–11), xSPEN relies on imprinting a shaped phase during an initial encoding process, which then serves as the focal point for a subsequent, gradient-driven image readout. In both experiments, this nonlinear phase encoding $\Phi_e(r)$ leads to destructive interferences among signals emitted from neighboring spins, except for those positioned close to positions fulfilling the stationary-phase condition $(\nabla\varphi_e)_{r=r_o}=0$. The action of an acquisition gradient, $G_a$, which provides to this initial encoding profile an additional evolution phase, $\varphi_a = k_a \cdot r$, with AQ9 $k_a=\gamma G_a t$ displaces this stationary phase point throughout the targeted field of view (FOV). If properly steered, AQ10 this will eventually reveal the full $\rho(r)$ spin density over the targeted FOV during a time-domain acquisition. Both SPEN and xSPEN thus differ from echo planar imaging (EPI, (12,13)) in that their image readout occurs in direct, physical space.

SPEN imparts its encoding as a quadratic, $y^2$, phase modulation, whereas xSPEN relies on a *y. z*-type phase AQ11 (1,14). When applying such hyperbolic encoding, the option arises of activating either the $G_a^y$ or $G_a^z$ acquisition gradients to unravel, respectively, either the $\rho(z)$ or the $\rho(y)$ spatial profiles. The physical basis of how these acquisition gradients allow one to read, in direct space, the spins' profile along an orthogonal axis has been explained elsewhere (1). Such analysis also reveals that utilizing a *z*-axis gradient to both encode and unravel a $\rho(y)$ image enables one to perform an acquisition that can be entirely free from chemical shift or field inhomogeneity effects. This reflects that, rather than viewing frequency dispersions as artifacts that need to be overcome by application of an overpowering external field gradient, this approach to MRI incorporates any disturbing frequency broadening as part of both the initial phase encoding and the subsequent image decoding processes. This capability is particularly valuable when considering single-shot 2D acquisitions, experiments that although central in numerous diffusion- and functional-oriented applications are known to be particularly sensitive to field inhomogeneity distortions (15–17). Figure 1a illus- F1 trates one method whereby the xSPEN strategy was AQ12 adapted for the realization of such single-shot 2D acquisitions. This sequence imparts its hyperbolic phase encoding by turning on a $G_z$ along the slice-selection axis; this is used for exciting a slice of width $L_z$ and is kept on throughout the rest of the scan. In combination with two linearly swept adiabatic inversion pulses (5,18) applied in the presence of a bipolar gradient $\pm G_y$, this results in xSPEN's characteristic $\Phi_e = -Cy.\ z$ phase pro- AQ14 AQ13 file, in which $C$ is a spatiotemporal encoding constant under the experimentalist's control and *y,z* are positions in the $-FOV_y/2 \le y \le FOV_y/2,\ -L_z/2 \le z \le L_z/2$ ranges. AQ15 Then, over the course of the acquisition, the continued action of the constant $G_z$ displaces $\Phi_e$'s saddle-shaped profile along the *y*-axis. In synchrony with this, an

Department of Chemical Physics, Weizmann Institute of Science, Rehovot, Israel.

Grant sponsors: Financial support from the Israel Science Foundation grant 795/13; the EU through ERC-2016-PoC grant 751106; Minerva funding (712277) from the Federal German Ministry for Education and Research; the Kimmel Institute for Magnetic Resonance; and the generosity of the AQ1 Perlman Family Foundation.

AQ6 *Correspondence to: Prof. Lucio Frydman, Department of Chemical Physics, Weizmann Institute of Science, 205 Herzl Street, Rehovot 76100, Israel. AQ2 AQ3 AQ4 AQ5 E-mail: lucio.frydman@weizmann.ac.il.

Received 20 March 2017; revised 11 June 2017; accepted 12 June 2017
DOI 10.1002/mrm.26824
Published online 00 Month 2017 in Wiley Online Library (wileyonlinelibrary.com).

J_ID: MRM Customer A_ID: MRM26824 Cadmus Art: MRM26824 Ed. Ref. No.: 17-17848.R2 Date: 30-June-17 Stage: Page: 2



oscillating $\pm G_x$ gradient applied along an orthogonal readout dimension explores the $k_x$-axis in a conventional, EPI-like manner. The mechanism by which the constant application of a $G_z$ gradient delivers an image free from offset-derived in-plane distortions has been discussed in detail elsewhere (1,19). Basically, even in the presence of a shift or inhomogeneity $\delta\omega(r)$, the xSPEN signal collected as a function of the oscillating wavenumber $k_x$ and the acquisition time $t$ can be expressed as

$$S(k_x,t) = \int_X dx \cdot e^{ik_x x} \int_Y dy \cdot \rho(x,y) \cdot \frac{L_z}{1+f[\delta\omega]} \cdot \mathrm{sinc}\left[(-Cy+\gamma G_z t)\frac{L_z}{2}\right]. \quad [1]$$

Therefore, rearrangement of these data and 1D Fourier transformation (FT) along $k_x$ leads, apart from potential distortions related to the slice selection and represented by the function $f[\delta\omega]$, to a 2D $\rho(x,y)$ image as a function of $t$ that will be devoid from all offset-derived misregistrations.

Although delivering single-shot images devoid from in-plane distortions, xSPEN's lack of FT along the low bandwidth dimension carries substantial signal-to-noise ratio (SNR) penalties. These penalties are compounded by the constant $G_z$ gradient required by xSPEN, which being larger than a usual EPI phase-encoding gradient by a ratio $\approx \frac{FOV_y}{L_z}$, usually will be responsible for the diffusion-related losses of this technique. In the absence of inhomogeneities, this makes single-shot xSPEN less sensitive than methods such as EPI or even its SPEN predecessors—particularly if using the long acquisition times $T_a$ required for achieving high in-plane resolutions. A well-known route to alleviate such effects is the partial FT (pFT, (20,21)), an approach that leverages the properties of the image being sought to reduce the acquisition coverage along one of the $k$-domains. Indeed, given the real nature of the NMR spectral correlations, in principle it is possible to sample only half the extent of the full $k$-space and still achieve the same levels of spatial resolution that would arise from sampling a full $-k^{max} \le k \le k^{max}$ range of values (22,23). In practice, such maximal reduction in the sampled data rarely is achieved, and partial sampling factors $0.6 \le p \le 0.8$ are more common. The $T_a \rightarrow p.$). $T_a$ shortening of the overall acquisition times associated to this partial sampling can lead to a considerable reduction in relaxation and in diffusion-driven losses—particularly for constant-gradient sequences such as xSPEN. The question then arises of how to exploit these $k$-based phase-conjugation arguments in sequences that, like SPEN or xSPEN, are based on the hybrid sampling of $k_x$ and of $y$ -domains. The physical basis of pFT experiments along the readout and low-bandwidth dimensions, and demonstrations of pFT's usefulness to achieve resolutions that so far have been out of xSPEN's experimental reach, are presented below.

## METHODS

### Theoretical background

pFT seeks to retain spatial resolution, while reducing MRI's acquisition times, by estimating part of the $k$-space data using complex conjugation. Thus, although 1D MRI's inherent resolution depends on the maximal sampled wavenumber $|k^{max}|$, blurring will characterize magnitude images unless a symmetric $-k^{max} \le k \le +k^{max}$ region is sampled. pFT relies on the fact that $k$-domain data have to fulfill $S(-k) = [S(+k)]^*$ order to calculate the images that would arise from the full $-k^{max} \le k \le k^{max}$ support, while limiting actual samples to a $-(2p-1).k^{max} \le k \le k^{max}$, $0.5 \le p \le 1$ fraction (20,24). When extending these considerations from a 1D axis to a 2D plane, two potential strategies emerge. One is to exploit the $S(-k_x, -k_y) = [S(k_x,k_y)]^*$ symmetry along the directly detected readout domain; the other is to apply it along the phase-

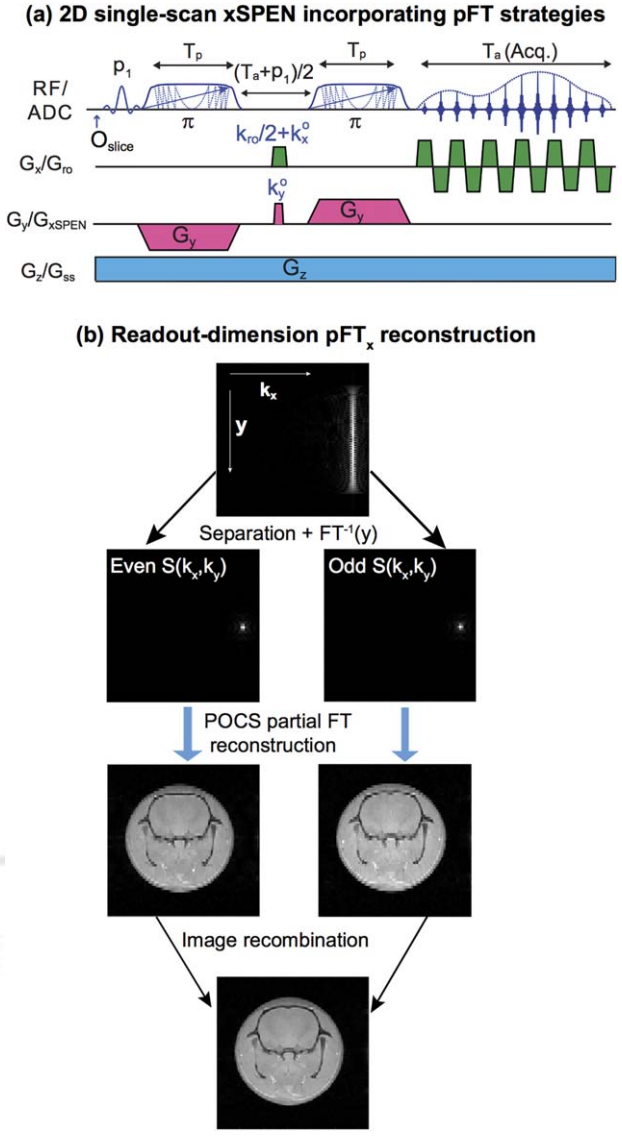


FIG. 1. (**a**) Single-shot xSPEN sequence incorporating partial Fourier acquisitions by adding short prephasing pulsed gradients along the readout ($pFT_x$) or xSPEN ($pFT_y$) axes. (**b**) $pFT_x$ reconstruction involving the addition of a $k_y^0$ gradient pulse that displaces the $S(k_x,y)$ interferogram (top), separate processing of even/odd $S(k_x,k_y)$ datasets via POCS reconstruction, and subsequent combination (interleaving of magnitude data in image space to avoid phase problems) of the two sets. FT, Fourier transform; pFT, partial Fourier transform; POCS, projection onto convex sets; RF, radiofrequency; xSPEN, cross-term spatiotemporal encoding.

COLOR IN ONLINE AND PRINT

encoded dimension. In conventional multi-shot MRI, the latter is the preferred option because it may shorten by a factor $p$ the duration of the experiment. Single-shot techniques such as EPI generally also apply pFT only along the phase-encoded domain because doing so along the readout axis tends to complicate even/odd artifact corrections. In single-shot xSPEN, the readout ($x$) dimension is $k$-based, and these even/odd complications are absent because there is no FT along the low bandwidth ($y$) dimension. Consequently, $pFT_x$ in xSPEN is to some extent simpler than what generally is the case in EPI: xSPEN's $pFT_x$ simply does a 1D phase conjugate reconstruction separately on positive and negative $k_x$-axis acquisitions and then recombines the two datasets in image space without phase problems to deliver its image (Fig. 1b).

Less straightforward is envisioning how pFT could be exploited along the xSPEN $y$-dimension. As mentioned, single-shot xSPEN imparts a preacquisition hyperbolic phase-encoding $e^{-iCyz}$, the stationary point of which is shifted over the course of the acquisition by a constant $z$-gradient. Such gradient in essence performs an analog Fourier analysis of the encoded data, delivering a $y$-axis image while simultaneously removing all $\Delta B_o$ inhomogeneity effects. This in turn means that an inverse FT of the data collected while under the action of the $G_z$ gradient will be equivalent to a conventionally $k_y$-encoded MRI acquisition, with $k_y = -Cz$ being the Fourier-conjugate to the $y$-position. Therefore, in the same way that conventional pFT relies on breaking the echo symmetry of a $k_y$-domain acquisition by applying a prewinding $G_y$ gradient, performing an asymmetric encoding of the xSPEN image would demand the introduction of a prewinding $G_y$ pulse, even if the image is subsequently unraveled by the action of a $G_z$. Figure 1a highlights how this route to performing $pFT_y$ along the low-bandwidth dimension can be included in the original 2D sequence by introducing a short prephasing gradient pulse $k_y^0$. Such prephasing effectively shifts xSPEN's virtual $k_y$ encoding, thereby opening a route by enhancing the $y$-axis resolution via pFT. To see how this arises, we revisit Equation [1] in the absence of inhomogeneities for a 1D case that for simplicity ignores the $k_x$ readout dimension. Approximating the *sinc* function in that formula as

$$L_z \mathrm{sinc}\left[(-Cy+\gamma G_z t)\frac{L_z}{2}\right] \approx \int_{-\frac{L_z}{2}}^{+\frac{L_z}{2}} dz \cdot e^{i(-Cy+\gamma G_x t)z} \quad [2]$$

enables us to describe the effect of the prephasing pulsed gradient $K_y^0$ on the detected signal as

$$S[k_z(t)] = \int_Y dy \int_Z \rho(y) e^{-ik_y^0 y} e^{i(-Cy+k_z)z} dz \approx e^{-ik_y^0 y'} r(y') \quad [3]$$

where $y' = k_z/C$ is the coordinate decoded by the action of the acquisition wavenumber $k_z = \gamma G_z t$, and $r(y')$ is a function representing the xSPEN image, given by a convolution of the $\rho(y)$ spin density with the *sinc*-based sampling point spread function. The $e^{-ik_y^0 y'}$ prefactor clearly represents a shift in the $k_y$-space origin associated with $r(y')$'s inverse Fourier transform signal $S(k_y) \int_Y r(y') e^{ik_y y'} dy'$. In other words, if in conventional xSPEN the maximum $y$-axis spatial resolution is given by the *sinc*'s width $\frac{2}{CL_z}$, the equivalent $k_y$ sampling associated to the prefactor in Equation [3] will be shifted from $-CL_z/2 \le k_y \le CL_z/2$ to an interval of $-CL_z/2 + k_y^0 \le k_y \le CL_z/2 + k_y^0$. Hence, an inverse FT of the acquired xSPEN image, a suitable phase-conjugation processing, and a forward FT should yield images arising from an extended $k_y$ support and thus possessing an enhanced $y$-axis resolution.

Similar pFT considerations would apply to single-shot 2D experiments if the imaging processes along xSPEN and readout axes were fully decoupled; this would be the case if the $G_z$ acquisition gradient would be pulsed in between the bipolar readout gradients. In practice, however, it often is convenient to leave on $G_z$ continuously because this frees not only the low bandwidth but also the readout dimension from field inhomogeneity distortions. The simultaneous action associated with the oscillating $G_x$ readout and the constant $G_z$ gradients acting during xSPEN's 2D single-shot acquisition bring about new features that need to be corrected before attempting a $pFT_y$. For deriving these features and their corrections, we consider for simplicity an xSPEN evolution that is free from relaxation, diffusion, or field inhomogeneities. The full 2D signal observed in such experiments can be expressed as

$$S(k_x,k_z) = \begin{cases} S^{odd}(k_x,k_z) = \int_X \int_Y \int_Z \rho(x,y) e^{o\phi^{odd}} e^{-i(Cz\cdot y + k_y^0 y)} e^{ik_x x} e^{i(k_z z + \beta k_x z)} dx\, dy\, dz & \text{if } G_x \ge 0 \\ S^{even}(k_x,k_z) = \int_X \int_Y \int_Z \rho(x,y) e^{o\phi^{even}} e^{-i(Cz\cdot y + k_y^0 y)} e^{ik_x x} e^{i(k_z z + \beta k_x z)} dx\, dy\, dz & \text{if } G_x < 0. \end{cases} \quad [4]$$

Here, the integrals extend over the targeted slice and FOVs; $k_z$ and $k_x$ are the acquisition wavenumbers along the low-bandwidth and readout axes; $\beta$ is a zigzag factor (23,25) reflecting the fact that the $k_x$ wavenumber advances/recedes in conjunction with $k_z$ over the course of the readout oscillation; and $\phi^{odd}$, $\phi^{even}$ are unknown phase terms associated with imperfections in the readout gradients. To adapt the $s(k_y) = \int_Y r(y') e^{ik_y y'} dy'$ notation introduced above to this 2D sampling case, we introduce functions related to what would be the conventional $k$-space signal associated to this acquisition; that is,

$$\begin{aligned} S^{odd}(k_x,k_z) &= \int_X \int_Y \rho(x,y) e^{o\phi^{odd}} e^{ik_x x} e^{ik_y y} dx\, dy \\ S^{even}(k_x,k_z) &= \int_X \int_Y \rho(x,y) e^{o\phi^{even}} e^{ik_x x} e^{ik_y y} dx\, dy\,. \end{aligned} \quad [5]$$

J_ID: MRM Customer A_ID: MRM26824 Cadmus Art: MRM26824 Ed. Ref. No.: 17-17848.R2 Date: 30-June-17 Stage: Page: 4



These virtual signals arising from positive and negative readout gradients can be used to rewrite Equation [4] as

$$S(k_x,k_z)=\begin{cases} S^{odd}(k_x,k_z)=\int_Z S^{odd}(k_x,k_y+k_y^0)e^{i(k_z z+\beta k_x z)}dz \\ S^{even}(k_x,k_z)=\int_Z S^{even}(k_x,k_y+k_y^0)e^{i(k_z z+\beta k_x z)}dz \end{cases}. \quad [6]$$

Furthermore, because $k_z$ rasterizes the $y$-axis, this is equivalent to the mixed-domain interferogram

$$S(k_x,y')=\begin{cases} S^{odd}(k_x,y')=\int_{k_y} S^{odd}(k_x,k_y+k_y^0)e^{i(k_z y'+\beta k_y k_x/C)}dk_y \\ S^{even}(k_x,y')=\int_{k_y} S^{even}(k_x,k_y+k_y^0)e^{i(k_z y'+\beta k_y k_x/C)}dk_y. \end{cases} \quad [7]$$

where $y'=k_z/C$.

If not for the $\beta$-related terms, one could apply the same arguments that followed Equation [3] to justify the extraction from these data of a $pFT_y$-enhanced resolution. To appreciate the effects associated to the $\beta$-terms, we perform on Equation [7] a final change of variables $k_y'=k_y+k_y^0$:

$$S(k_x,y')=\begin{cases} S^{odd}(k_x,y')=e^{-ik_y^0 y'}e^{-i\beta k_x k_y^0/C}\int_{k_y'} S^{odd}(k_x,k_y')e^{ik_y'(y'+\beta k_x/C)}dk_y' \\ S^{even}(k_x,y')=e^{-ik_y^0 y'}e^{-i\beta k_x k_y^0/C}\int_{k_y'} S^{even}(k_x,k_y')e^{ik_y'(y'+\beta k_x/C)}dk_y' \end{cases} \quad [8]$$

The $e^{-ik_y^0 y'}$ phase-modulation term here is, as in conventional $pFT_y$; however, the new phase terms $e^{i\beta k_x k_y^0/C}$ and $e^{i\beta k_x k_y^0/C}$, affecting the $S^{even}$ and $S^{odd}$ interferograms, evidence a coupling between the $k_y^0$ echo shifts and the $k_x$ sampling that needs to be removed from even and odd data sets before performing a $pFT_y$. In practice, we apply this *zigzag correction*, involving a row-by-row multiplication of these a priori known $\beta$-phase terms, in conjunction with a removal of the $e^{i\phi^{odd}}$ and $e^{i\phi^{even}}$ phase imperfections that may affect signals collected under $\pm G_x$ gradients (23,26,27). The full procedure is summarized and exemplified in Figure 2. In the present study, the POCS (projection onto convex sets) partial Fourier reconstruction (28,29) was the pFT algorithm chosen to enhance resolution along either the readout or low-bandwidth axes.

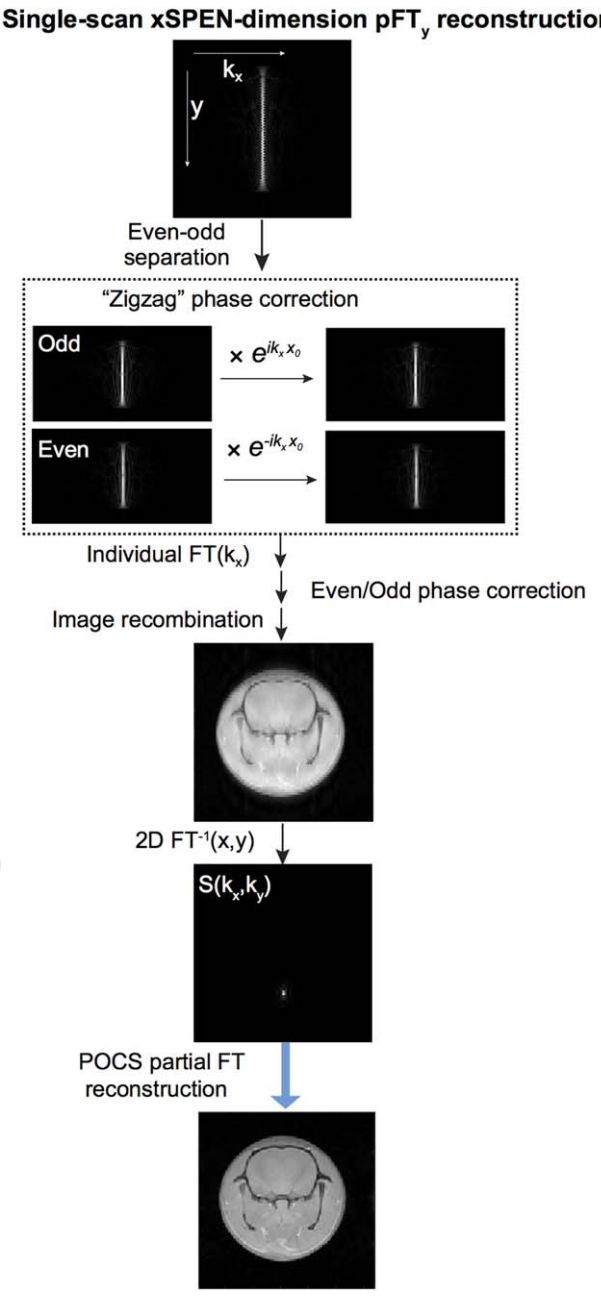


FIG. 2. $pFT_y$ reconstruction involving the addition of a $k_y^0$ gradient pulse that modulates the xSPEN $y$-image, separation of even/odd data sets, phase correction by a priori known zigzag effects $k_x x_o$ with $x_o=\beta k_y^0/C$, subsequent correction of residual even/odd phase problems, and final POCS-based partial FT reconstruction of the effective k-domain $S(k_x,k_y)$ data. Notice that whereas fixing even/odd phase problems was not essential in the original xSPEN experiment, if solely a 1D FT along the readout axis was involved, it becomes necessary when implementing the additional manipulations involved in the pFT. FT, Fourier transform; pFT, partial Fourier transform; POCS, projection onto convex sets; xSPEN, cross-term spatiotemporal encoding.

COLOR IN ONLINE AND PRINT

## Experimental

Phantom and animal-based acquisitions were carried out on a 7T/120 mm horizontal magnet using a quadrature volume coil and a DD2 Agilent console (Agilent Technologies, Santa Clara, California, USA). Animal protocols and maintenance were done in accordance with guidelines of the Institutional Committee on Animals of the Weizmann Institute of Science (protocol 10790514). Spin-echo multi-shot (SEMS) images and SE-EPI experiments were carried out using sequences taken from the scanner's library; all SE-EPI acquisitions required reference "navigator" scans to correct for ghosting along the

J_ID: MRM Customer A_ID: MRM26824 Cadmus Art: MRM26824 Ed. Ref. No.: 17-17848.R2 Date: 30-June-17 Stage: Page: 5





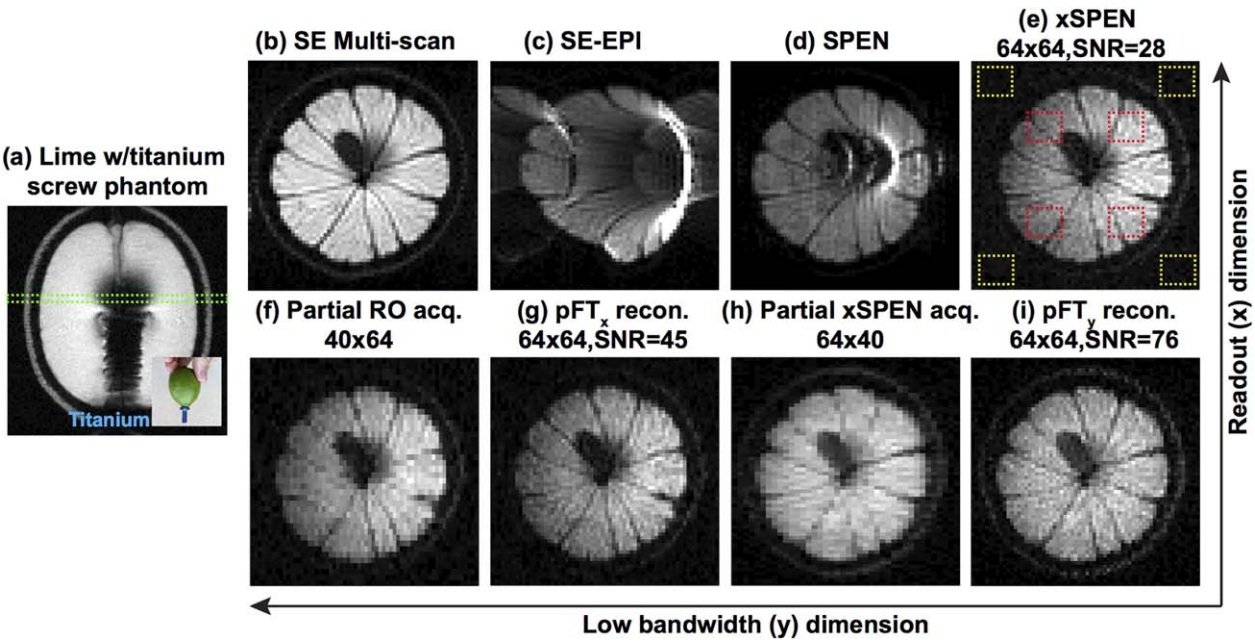


FIG. 3. Representative results arising from a lime phantom incorporating a titanium screw (**a**). (**b**) Spin-echo multi-shot image arising from the green axial slice indicated in (**a**). (**c–e**) 2D imaging results delivered for the same slice by different single-shot sequences with identical FOV and resolution settings. (**f**,**g**) Images from a same acquisition involving partial sampling of the readout dimension, processed with and without POCS reconstruction. (**h**,**i**) Idembut with and without $pFT_y$ reconstruction along the xSPEN dimension. Both (**g**) and (**i**) have the same resolution as (**e**) but higher SNR, as evaluated from averaged ratios of the yellow/red squares denoting noise/signal regions shown in panel (**e**). Acquisition parameters: FOV = $40 \times 40\,mm^2$; thickness = 4 mm; repetition time = 2 s; $T_a$ = 22.02, 15.88, and 13.76 ms for (**e**), (**f**), and (**h**); time-bandwidth products $2.G_eT_e = 64$, 64 and 40 for (**e**), (**f**), and (**h**); chirp bandwidths = 5.8, 8.0, and 5.8 kHz for (**e**), (**f**), and (**h**), respectively. Matrix sizes for images in (**b–d**) were $64 \times 64$; xSPEN image sizes were as indicated. EPI, echo-planar imaging; FOV, field of view; pFT, partial Fourier transform; RO, readout; SE spin echo; SNR, signal-to-noise-ratio; xSPEN, cross-term spatiotemporal encoding.



phase-encoded dimensions. SPEN and xSPEN imaging experiments were run in this preclinical scanner using custom-written pulse sequences and processing macros that were integrated into Agilent/Varian's VNMRJ (Agilent Technologies) imaging software; these are available upon request. Human volunteers were scanned on a 3T Siemens TIM TRIO platform (Siemens Healthcare, Erlangen, Germany) using a 32-channels head coil. Compared in these scans were SE-EPI sequences taken from the scanner's library against custom-written xSPEN acquisition/processing programs. These experiments were approved by the internal review board WOMC-0091-11 of the Wolfson Medical Center (Holon, Israel) and collected after obtaining informed suitable consents. Main parameters used for setting up the various experiments are detailed in the corresponding figure captions.

## RESULTS

Figure 3 illustrates the advantages resulting from the pFT procedures just discussed, when performed on a 7T preclinical scanner. In these experiments, a lime was analyzed, onto which a nonferromagnetic titanium screw of a kind usually employed in orthopedic prostheses was inserted axially for exacerbating the field inhomogeneities. Figure 3a shows a photograph of the screw plus fruit, together with a SEMS sagittal image showing the effects of the screw as well as a challenging slice on which further axial analyses where implemented. These compared a SEMS image (usually used as our gold standard) (Fig. 3b) and images collected with SE-EPI with fully refocused SPEN and with the xSPEN sequence introduced in (1). This progression clearly shows the latter's higher robustness and faithfulness (Figs. 3c–3e). Using this single-shot xSPEN image collected with the original sequence as starting point, Figures 3f through 3i illustrate the kind of improvements that can be achieved by implementing pFT procedures. Figures 3f and 3g show images obtained upon reducing the number of points collected along xSPEN's readout segments from 64 to 40. Although a simple $FT_x$ procedure yields a lower resolution vis-à-vis the original 64-points xSPEN acquisition, the $pFT_x$ processing clearly restores this resolution. At the same time, the shortened echo times brought about by the $p = 0.625$ reduction in readout points clearly improves the sensitivity. An even larger sensitivity improvement is observed for identical $P$ values if the pFT is implemented along the low-bandwidth dimension. Indeed, although Figure 3h once again shows that resolution is sacrificed upon reducing the sampled xSPEN lines from 64→40, the procedure in Figure 2 can restore the lost resolution while nearly tripling SNR vis-à-vis the original single-shot xSPEN image (Fig. 3i vs. 3e).

Figure 4 demonstrates another aspect of pFT's sensitivity improvements, this time focusing on tradeoffs between resolution and SNR. Shown in the first row are images recorded for the phantom and slice introduced in

ID: thangaraj.n Time: 22:19 I Path: //chenas03/Cenpro/ApplicationFiles/Journals/Wiley/MRMT/Vol00000/170202/Comp/APPFile/JW-MRMT170202

J_ID: MRM Customer A_ID: MRM26824 Cadmus Art: MRM26824 Ed. Ref. No.: 17-17848.R2 Date: 30-June-17 Stage: Page: 6





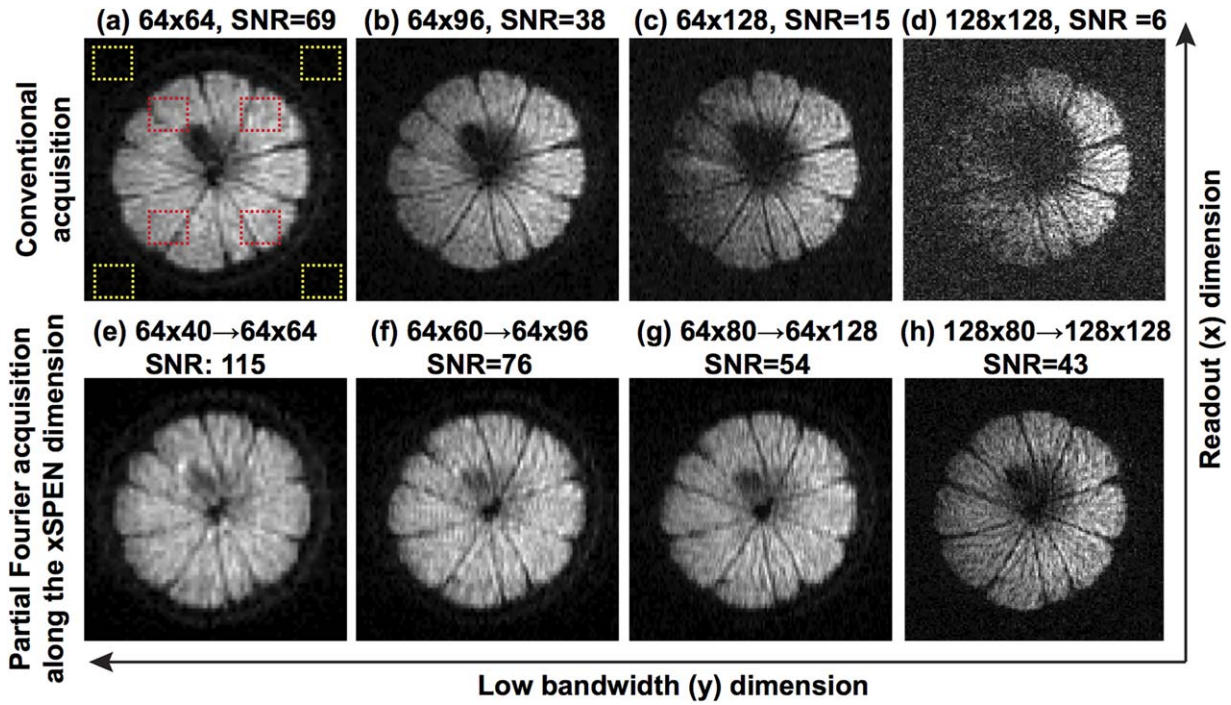


FIG. 4. Sensitivity benefits arising from partial Fourier processing along the xSPEN dimension ($pFT_y$), as judged by the SNR figures arising from the indicated yellow/red squares on the phantom introduced in Figure 3. (**a–d**) Images acquired with conventional xSPEN, showing how SNR degrades with increasing image resolution due to longer $T_a$s and associated diffusion losses. (**e–h**) $pFT_y$ reconstructed counterparts showing how SNR gains improve with resolution. Acquisition parameters field of view = $40 \times 40\,mm^2$; thickness = 4 mm; repetition time = 2 s; $T_a$ = 22.02, 33.02, 44.03, 76.8, 13.76, 20.64, 27.52, and 48 ms for (**a–h**); time-bandwidth products = 64, 96, 128, 128, 40, 60, 80, and 80 for (**a–h**); and chirp bandwidths = 5.8, 5.8, 5.8, 3.3, 5.8, 5.8, 5.8, and 3.3 kHz for (**a–h**), respectively. Matrix sizes were as indicated (arrows indicate the extent of the augmentation brought about by the pFT procedure). pFT, partial Fourier transform; SNR, signal-to-noise-ratio; xSPEN, cross-term spatiotemporal encoding.



Figure 3b, using the original xSPEN sequence as function of increasing matrix size. This quickly trades SNR for resolution (Figs. 4a–4d), reflecting in part the decreasing voxel sizes, but foremost the diffusion and relaxation penalties incurred upon seeking to increase resolution along the low bandwidth dimension. Images reconstructed using $pFT_y$ clearly can increase SNR vis-a-vis conventionally acquired xSPEN counterparts (Figs. 4e–4h). Moreover, the higher the resolution desired, the larger the SNR benefits arising from relying on a pFT.



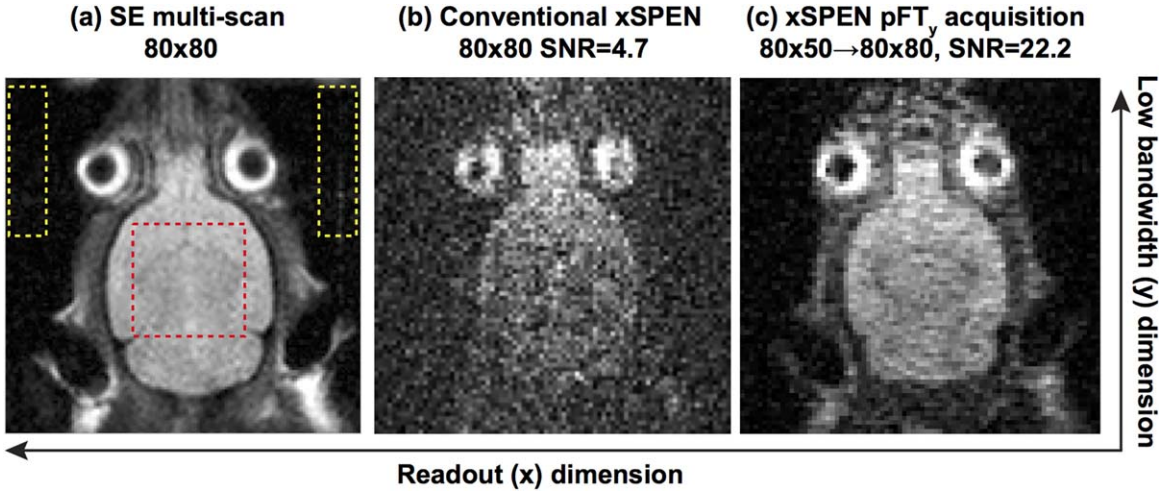


FIG. 5. Sensitivity benefits arising from xSPEN's $pFT_y$, illustrated with in vivo mouse head scans. (**a**) Reference spin-echo multi-shot image acquired in 2 min 40 s without respiration trigger, and indicating the regions used to evaluate signal (yellow) and noise (red). Images with lower and with improved SNR acquired by single-shot xSPEN MRI without (**b**) and with (**c**) pFT to deliver the same resolution. Field of view = $24 \times 24\,mm^2$; slice thickness = 2.5 mm; repetition time = 2 s; $T_a$ = 32.6 and 20.4 ms; time-bandwidth products = 80, 50 and chirp bandwidths 4.8, 4.8 kHz for (**b**) and (**c**), respectively. Matrix sizes as indicated. pFT, partial Fourier transform; SE spin echo; SNR, signal-to-noise-ratio; xSPEN, cross-term spatiotemporal encoding.

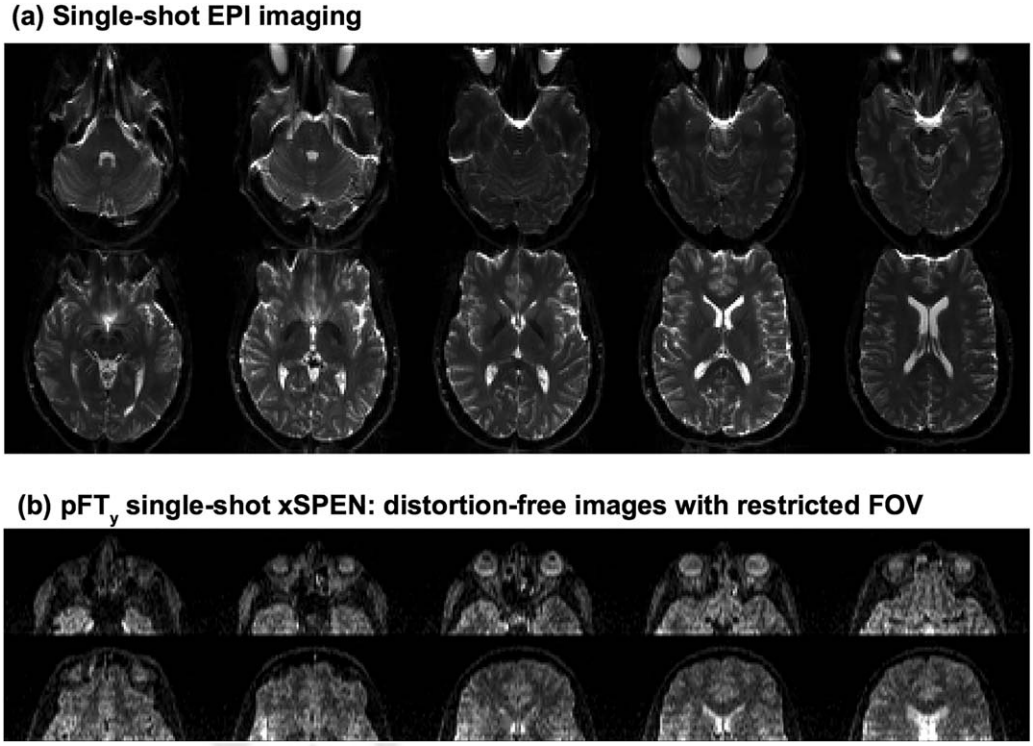


FIG. 6. (**a**) Multislice single-shot EPI images (TR = 2 s) collected on a human volunteer at 3T. FOV = $192 \times 192\,mm^2$, matrix size = $96 \times 96$, echo time = 77 ms, and $T_a = 72.96$ ms. (**b**) Corresponding single-shot xSPEN images arising from the same volunteer upon performing a partial FT scan (TR = 4 s) along the spatiotemporal dimension. FOV = 192(RO) × 96(xSPEN) $mm^2$, matrix size = $96 \times 30$ reconstructed into a $96 \times 48$ array by pFT$_y$, $T_a = 22.08$ ms, time-bandwidth product = 30, and chirp bandwidth = 2.7 kHz. All images possess identical $2 \times 2\,mm^2$ in-plane resolutions. EPI, echoplanar imaging; FOV, field of view; pFT, partial Fourier transform; RO, readout; TR, repetition time; xSPEN, cross-term spatiotemporal encoding.



F5 These advantages are recapitulated in Figure 5, with in vivo experiments comparing SEMS data against single-shot xSPEN images targeting a mouse head. Notice the absence of distortions in regions that typically challenge single-shot applications, for example, near eyeballs and in the ears. Notice as well the large ($\geq 5\times$) SNR improvements brought about by the pFT$_y$ procedure for the $p = 0.625$ and $300 \times 300\,\mu m^2$ in-plane resolution targeted
F6 here. Figure 6 illustrates a similar advantage, but for a series of scans collected at 3T on a human volunteer and focusing on the frontal orbital cortex. Due to the susceptibility gradients introduced by the sinuses and eye sockets, single-shot EPI exhibits substantial distortions over various head regions (Fig. 6a). xSPEN yields distortion-less images for these regions, but the strong diffusion-driven losses arising when seeking in-plane resolutions better than $2 \times 2\,mm^2$ render this approach of limited value—even if restricting the FOV to limit the overall acquisition times (data not shown). By contrast, pFT$_y$ enables xSPEN to successfully target this resolution: by sampling only 62.5% of the readout lines, this procedure achieves acceptable SNR and yields undistorted, single-shot zoomed images, free from folding and/or susceptibility artifacts (Fig. 6b).

## DISCUSSION

Single-scan xSPEN MRI shows remarkable resilience to field inhomogeneities yet suffers from SNR penalties due to its non-Fourier nature and diffusion and $T_2$ losses. These losses can be taxing when seeking improvements along the spatiotemporally encoded dimension, for which resolution is given by $\delta y = \frac{2\pi FOV}{T_a \cdot \gamma G_z L_z}$ (1). $\delta y$ can thus be improved by restricting $FOV_y$ or by increasing the slice thickness $L_z$, albeit at the expense of losing in- or AQ34 out-of-plane information. Additional parameters available for increasing resolution are $G_z$, the gradient that in AQ35 xSPEN stays on for the course of the scan, and the acquisition time $T_a$. Owing to xSPEN's refocusing demands, $T_a$ will be proportional to each voxel's position-dependent echo time TE, and hence impart an $e^{-TE/T_2} = e^{-(\alpha T_a)/T_2}$ attenuation for which $\alpha$ is a factor ranging between 2 and 3, and depending on the voxel's $y$-position. Improving resolution by increasing either $G_z$ or AQ36 $T_a$ will incur in diffusion losses. Based on the Bloch-Torrey model (30,31), these losses can be approximated by an exponential attenuation varying as the square of the gradient and the cube of the free evolution time. On the basis of this, and disregarding for simplicity the effects of the refocusing pulses or of the $\pm G_y$ encoding and $\pm G_x$ readout gradients, xSPEN's diffusion-driven attenuation will be proportional to $e^{-D\gamma^2 G_z^2 (\alpha \cdot T_a)^3/12}$, with $D$ the diffusion coefficient.

pFT decreases these sensitivity losses without sacrificing resolution by collecting a fraction $p < 1$ of the points that would normally be required. This will result in shortened acquisition times that can be implemented by partially sampling either the readout ($x$) or the

J_ID: MRM Customer A_ID: MRM26824 Cadmus Art: MRM26824 Ed. Ref. No.: 17-17848.R2 Date: 30-June-17 Stage: Page: 8



spatiotemporally encoded ($y$) dimensions. The first of these options restores the original $x$-axis resolution while acquiring a fraction of the original readout points. Disregarding for simplicity complications associated to ramp sampling or finite gradient slew rates, reducing the number of sampled readout points by a factor of $p<1$ will shorten accordingly the associated acquisition time $T_a$, leading to a reduction of the $T_2$-driven relaxation losses by $e^{-p(\alpha\cdot T_a)/T_2}$. However, if this is to be done without a concomitant loss in the $y$-axis resolution, the relation given earlier for $\delta y$ implies that $G_z$ will have to increase by a factor $1/p$. The ensuing diffusion-related attenuation factor will therefore be reduced to $e^{-p\cdot D\gamma^2 G_z^2(\alpha\cdot T_a)^3/12}$; because $p<1$, this is clearly an improvement over the original attenuation. Compare this with the case of $pFT_y$, in which the $T_a$ reduction is achieved by sampling fewer points along $y$-axis—that is, by applying fewer $\pm G_x$ readout oscillations. The reduction in $T_2$-driven attenuation losses will remain as for $pFT_x$; however, the fact that the $G_z$ can now be kept at its original strength without incurring in a $\delta y$-degradation means that the diffusion-driven attenuation factor will be reduced to $e^{-p^3\cdot D\gamma^2 G_z^2(\alpha\cdot T_a)^3/12}$. Therefore, although both $pFT_x$ and $pFT_y$ will improve SNR over xSPEN's original realization, $pFT_y$ will lead to a larger improvement due to the $p^3<p<1$ factor arising in the diffusion-weighting exponent. This advantage of $pFT_y$ over $pFT_x$ is compounded by xSPEN's lack of Fourier transform along the xSPEN dimension, which makes the sensitivity of the overall method drop as [# sampled points]$^{1/2}$. By reducing this number by a factor $p$, adopting the pFTy procedure enhances sensitivity by another factor $1/\sqrt{p}$. All these expectations are confirmed by the data in Figure 3. They also explain the observations in Figure 4 whereby the higher the resolution being sought, the more there is to be gained by adopting the $pFT_y$ procedure. Indeed, in the latter case the increases in resolution called for the use of longer encoding and acquisition times that rapidly increased the diffusion-related attenuation exponent; the larger this exponent, the more remarkable are the benefits of the $p^3$ $pFT_y$ scaling in the final image SNR. Although an exact quantification of the SNR enhancement introduced by the pFT might benefit from synthetic replica procedures, the large factors evidenced by the experimental data demonstrate the method's usefulness.

In addition to pure SNR considerations, a number of technical factors point to the convenience of choosing partial Fourier sampling along the spatiotemporal rather than the readout axis, particularly when considering xSPEN realizations on humans. One of these pertains to the limited $p$ reductions that can be achieved in clinical scanners along the readout axis, where minimum readout times already are constrained by the maximal slew rates that physiological considerations allow one to achieve. Another limitation derives from the aforementioned need to increase the value of $G_z$ by $1/p$ upon performing $pFT_x$ without decreasing the $y$-axis resolution. This gradient increase means that chirped pulses with larger bandwidths are needed to cover the original $FOV_y$ and $L_z$ dimensions, resulting in concomitant increases in xSPEN's SAR values. In terms of data postprocessing, however, the reverse considerations apply: $pFT_x$ will barely change the original simplicity of the xSPEN processing, whereas $pFT_y$ requires both even/odd and zigzag phase corrections. Furthermore, to some extent there is an approximation in the assumption made in Figure 2 that these two corrections can be treated independently: a more rigorous analysis of even/odd mismatch problems incorporating the zigzag effect suggests that it may not always be feasible to factor out the phase terms $e^{\pm i\beta k_x k_y^0/C}$ from the integrals introduced in Equation [8]. When this is the case—and this naturally will depend on the nature of the even/odd mismatches—artifacts may arise in images processed, as described above. A general solution to this problem consists of replacing the continuous $G_z$-driven xSPEN decoding by equivalent gradient blips, acting during the ramp times of the oscillating readout gradient train.

## CONCLUSION

In summary, partial FT approaches acting along either the readout or the spatiotemporally encoded dimensions were introduced and shown to significantly improve the tradeoffs between resolution and SNR in single-scan xSPEN MRI. Details on how to implement these approaches were derived, and associated data processing considerations were introduced. In all cases, examples collected on preclinical and clinical scanners unambiguously demonstrate the advantages of the method without affecting xSPEN's unique resilience to field inhomogeneities. From a practical standpoint, this should readily benefit the potential applications of this new single-scan technique. From a conceptual standpoint, new physical insight had to be introduced in connection to the $pFT_y$, dealing with the application of orthogonal gradients to $k$-shift and to acquire a given imaging axis. These insights can in fact be extended to derive altogether new sampling schemes for single- and multi-shot xSPEN, as will be further detailed in upcoming studies.

## ACKNOWLEDGMENT

We are grateful to Dr. Sagit Shushan (Wolfson Medical Center) and Edna Furman-Haran (Weizmann) for assistance in the human scans, and to Dr. Gilad Liberman (Weizmann) for assistance in the coding of the 3T experiments. Z.Z. thanks Israel's Council of Higher Education and the Koshland Foundation for partial postdoctoral fellowships.

## REFERENCES

1. Zhang Z, Seginer A, Frydman L. Single-scan MRI with exceptional resilience to field heterogeneities. Magn Reson Med 2017;77:623–634.
2. Shrot Y, Frydman L. Spatially encoded NMR and the acquisition of 2D magnetic resonance images within a single scan. J Magn Reson 2005;172:179–190.
3. Tal A, Frydman L. Spatial encoding and the single-scan acquisition of high definition MR images in inhomogeneous fields. J Magn Reson 2006;182:179–194.
4. Chamberlain R, Park JY, Corum C, Yacoub E, Ugurbil K, Jack CR Jr, Garwood M. RASER: a new ultrafast magnetic resonance imaging method. Magn Reson Med 2007;58:794–799.
5. Tal A, Frydman L. Single-scan multidimensional magnetic resonance. Prog Nucl Magn Reson Spectrosc 2010;57:241–292.

6. Ben-Eliezer N, Shrot Y, Frydman L. High-definition, single-scan 2D MRI in inhomogeneous fields using spatial encoding methods. Magn Reson Imaging 2010;28:77–86.
7. Chen Y, Li J, Qu X, Chen L, Cai C, Cai S, Zhong J, Chen Z. Partial Fourier transform reconstruction for single-shot MRI with linear frequency-swept excitation. Magn Reson Med 2013;69:1326–1336.
8. Chen L, Bao L, Li J, Cai S, Cai C, Chen Z. An aliasing artifacts reducing approach with random undersampling for spatiotemporally encoded single-shot MRI. J Magn Reson 2013;237:115–124.
9. Cai C, Dong J, Cai S, Li J, Chen Y, Bao L, Chen Z. An efficient deconvolution reconstruction method for spatiotemporal-encoding single-scan 2D MRI. J Magn Reson 2013;228:136–147.
10. Schmidt R, Frydman L. New spatiotemporal approaches for fully refocused, multislice ultrafast 2D MRI. Magn Reson Med 2014;71: 711–722.
11. Zhang Z, Frydman L. MRSI via fully-refocused spatiotemporal encoding with polychromatic spectral pulses. J Magn Reson 2015;259:24–31.
12. Mansfield P. Multi-planar image-formation using NMR spin echoes. J Phys C: Solid State Phys 1977;10:L55–L58.
13. Stehling MK, Turner R, Mansfield P. Echo-planar imaging: magnetic resonance imaging in a fraction of a second. Science 1991;254:43–50.
14. Paquin R, Pelupessy P, Bodenhausen G. Cross-encoded magnetic resonance imaging in inhomogeneous fields. J Magn Reson 2009;201: 199–204.
15. Jezzard P, Balaban RS. Correction for geometric distortion in echo planar images from B0 field variations. Magn Reson Med 1995;34:65–73.
16. Hennel F. Multiple-shot echo-planar imaging. Concepts Magn Reson 1997;9:43–58.
17. Schmitt F, Stehling MK, Turner R. Echo-Planar Imaging: Theory, Technique and Application. Berlin, Germany: Springer; 2012.
18. Pelupessy P. Adiabatic single scan two-dimensional NMR spectroscopy. J Am Chem Soc 2003;125:12345–12350.
19. Pelupessy P, Rennella E, Bodenhausen G. High-resolution NMR in magnetic fields with unknown spatiotemporal variations. Science 2009;324:1693–1697.
20. Feinberg DA, Hale JD, Watts JC, Kaufman L, Mark A. Halving MR imaging time by conjugation: demonstration at 3.5 kg. Radiology 1986;161:527–531.
21. MacFall JR, Pelc NJ, Vavrek RM. Correction of spatially dependent phase shifts for partial fourier imaging. Magn Reson Imaging 1988;6: 143–155.
22. Ernst RR, Bodenhausen G, Wokaun A. Principles of Nuclear Magnetic Resonance in One and Two Dimensions. Oxford, UK: Clarendon Press; 1987.
23. Bernstein MA, King KF, Zhou XJ. Handbook of MRI Pulse Sequences. Burlington, MA: Elsevier Academic Press; 2004.
24. Bracewell RN. The Fourier Transform and its Application. New York, NY: McGraw-Hill; 1978.
25. Yan H, Braun M. Image reconstruction from Fourier domain data sampled along a zig-zag trajectory. Magn Reson Med 1991;18:405–410.
26. Buonocore MH, Gao L. Ghost artifact reduction for echo planar imaging using image phase correction. Magn Reson Med 1997;38:89–100.
27. Seginer A, Schmidt R, Leftin A, Solomon E, Frydman L. Reference-less reconstruction of spatiotemporally encoded imaging data: principles and applications to real-time MRI. Magn Reson Med 2014;72: 1687–1695.
28. Haacke EM, Lindskogj ED, Lin W. A fast, iterative, partial-Fourier technique capable of local phase recovery. J Magn Reson 1991;92:126–145.
29. Liang Z-P, Lauterbur PC. Principles of Magnetic Resonance Imaging: A Signal Processing Perspective. New York, NY: IEEE Press Series on Biomedical Engineering; 1999.
30. Torrey HC. Bloch equations with diffusion terms. Phys Rev 1956;104: 563.
31. Stejskal EO, Tanner JE. Spin diffusion measurements: spin echoes in the presence of a time-dependent field gradient. J Chem Phys 1965; 42:288–292.


AQ42

AQ1: AU: Please confirm that financial support footnote is correct as set. Update as needed (see Acknowledgments.)

AQ2: AU: Please confirm mailing address taken from transmittal sheet.

AQ3: AU: Please confirm that correspondence footnote is correct as set.

AQ4: AU: If desired, please provide the Corresponding Author's Twitter handle (@handle).

AQ5: AU: Abbreviations list, which is not part of journal style, was deleted.

AQ6: AU: Review article carefully. As needed, abbreviations deleted at only mention and expanded at first mention.

AQ7: AU: Abbreviation SNR spelled out at only mention in Abstract.

AQ8: AU: Note that single-shot MRI, resolution enhancement, and sensitivity enhancement do not appear in this article.

AQ9: AU: Check for accuracy. There is a superscript period here. Should it be deleted or revised?

AQ10: AU: Meaning of original unclear. Check revised for accuracy and modify as needed.

AQ11: AU: Check for accuracy. There is a superscript period here. Should it be deleted or revised?

AQ12: AU: OK as revised?

AQ13: AU: Check for accuracy. Should this be revised as a minus sign?

AQ14: AU: Check for accuracy. There is a superscript period here. Should it be deleted or revised?

AQ15: AU: Should these dashes be revised as minus symbols. Also, spacing revised for clarity. OK?

AQ16: AU: If possible, move punctuation (period or comma) after equation to other side of equation number (e.g., [1].) See other equations as well.

AQ17: AU: Larger than a typical?

AQ18: AU: En dash in –kmax revised with minus symbol ($-k^{max}$) throughout. OK?

AQ19: AU: Check throughout of accuracy ($p$ factor; $P$ value) and revise as needed.

AQ20: AU: Check for accuracy. There is a superscript period here and another after $p$. Should they be deleted or revised?

AQ21: AU: Should this be revised as $k_y$?

AQ22: AU: Check for accuracy. Should dashes be revised as minus sign and hyphen as en-dash? Also, there is a superscript period here. Should it be deleted or revised?

AQ23: AU: Rephrase "simply does"

AQ24: AU: Confirm punctuation in $e^{-icyz}$.

AQ25: AU: OK as revised to avoid repetition (associated to/associated to) in sentence?

AQ26: Here is what? Please clarify.

AQ27: This sentence does not make sense. Could it be revised as "The $e^{-ik_y^0 y'}$ phase-modulation term here is [content appears to be missing here], as in conventional $pFT_y$; however, the new phase terms $e^{i\beta k_x k_y^0/C}$ and $e^{i\beta k_x k_y^0/C}$, affecting the Seven and Sodd interferograms evidence a coupling between the $k_y^0$ echo shifts and the kx sampling that must be removed from even and odd data sets before performing a pFTy"? See revised punctuation and note comment about missing text.

AQ28: AU: Abbreviation IACUC deleted at only mention in article.

AQ29: AU: Confirm accuracy.

AQ30: AU: Confirm accuracy.

AQ31: AU: Perhaps clarify as "one lime" or "an average-sized lime."

AQ32: AU: OK as revised?

AQ33: AU: Perhaps revise as "screw plus fruit (lime)."

AQ34: AU: Confirm that you meant losing.

AQ35: AU: Please clarify. Remains during? Remains constant during?

AQ36: AU: Check for consistency. Proportional to each voxel's position-dependent echo time TE ... and based on each voxel's *y*-position?

AQ37: AU: no.?

AQ38: AU: Meaning of original unclear. OK as revised, or is text missing from the original?

AQ39: AU: Per journal style, CONCLUSION head should be separate. Please confirm or change location where it was placed.

AQ40: AU: Financial information moved to footnote. If council or foundation provided funding, update funding section of title page footnote.

AQ41: AU: Please review references carefully.

AQ42: AU: Review figure legends carefully to ensure accuracy of final content. Update abbreviation lists as needed.

AQ43: AU: Add ADC to list. Analog-to-digital?

AQ44: AU: Check "idem" for accuracy.

AQ45: AU: Check for accuracy. There is a superscript period here. Should it be deleted or revised?

AQ46: Please confirm that given names (red) and surnames/family names (green) have been identified correctly.

## Funding Info Query Form

Please confirm that the funding sponsor list below was correctly extracted from your article: that it includes all funders and that the text has been matched to the correct FundRef Registry organization names. If a name was not found in the FundRef registry, it may be not the canonical name form or it may be a program name rather than an

organization name, or it may be an organization not yet included in FundRef Registry. If you know of another name form or a parent organization name for a "not found" item on this list below, please share that information.

| **FundRef name** | **FundRef Organization Name** |
|---|---|
| Israel Science Foundation | [NOT FOUND IN FUNDREF REGISTRY] |
| ERC-2016-PoC | [NOT FOUND IN FUNDREF REGISTRY] |
| Minerva funding | [NOT FOUND IN FUNDREF REGISTRY] |
| Federal German Ministry for Education and Research | [NOT FOUND IN FUNDREF REGISTRY] |
| Kimmel Institute for Magnetic Resonance | [NOT FOUND IN FUNDREF REGISTRY] |
| Perlman Family Foundation. | [NOT FOUND IN FUNDREF REGISTRY] |